Suprathermal electron penetration into the inner magnetosphere of Saturn

M. F. Thomsen[(1)], A. J. Coates[(2)], E. Roussos[(3)], R. J. Wilson[(4)],
K. C. Hansen[(5)], and G. R. Lewis[(2)]

[(1)] Planetary Science Institute, 1700 East Fort Lowell, Suite 106, Tucson, AZ, USA 85719
[(2)] Mullard Space Science Laboratory, University College London, Dorking, UK
[(3)] Max Planck Institute for Solar System Research, Goettingen, Germany
[(4)] Laboratory for Atmospheric and Space Physics, University of Colorado, Boulder, CO, USA
[(5)] Climate and Space Sciences and Engineering, University of Michigan, Ann Arbor, MI, USA

Key Points:

- In Saturn's inner magnetosphere, the hot-electron population largely disappears inside of L=Lc.
- Lc varies greatly from pass to pass on timescales of 10 h or less.
- 90% of Lc values lie between 4.7 and 8.4, with median of 6.2.

Abstract

For most Cassini passes through the inner magnetosphere of Saturn, the hot-electron population (> few hundred eV) largely disappears inside of some cut-off L-shell. Anode-and-actuation-angle averages of hot-electron fluxes observed by the Cassini Electron Spectrometer (ELS) are binned into 0.1-R_s bins in dipole L to explore the properties of this cutoff distance. The cut-off L-shell is quite variable from pass to pass (on time scales as short as 10-20 h). At energies of 5797 eV, 2054 eV, and 728 eV, 90% of the inner boundary values lie between L~4.7 and 8.4, with a median near L=6.2, consistent with the range of L values over which discrete interchange injections have been observed, thus strengthening the case that the interchange process is responsible for delivering the bulk of the hot electrons seen in the inner magnetosphere. The occurrence distribution of the inner boundary is more sharply peaked on the night side than at other local times. There is no apparent dependence of the depth of penetration on large-scale solar wind properties. It appears likely that internal processes (magnetic stress on mass-loaded flux tubes) are dominating the injection of hot electrons into the inner magnetosphere.

Index Terms: 2756, 2730, 2740, 2764

Key Words: Saturn’s magnetosphere, interchange injections

1. Introduction

The plasma content of the inner magnetosphere of Saturn (inside of L~10, where L is the equatorial crossing point in R_s of a dipole magnetic field line) is a combination of cool, dense plasma that originated in water gas and ice emitted by the moon Enceladus, extremely high-energy radiation belt particles, and a suprathermal population that exists in the energy range between the dense plasma and the high-energy particles. The suprathermal population, which is presumably the source for the radiation belts, appears to originate in the outer magnetosphere, perhaps by processes associated with magnetic reconnection in the magnetotail. The electron portion of this population shows evidence of roughly adiabatic transport from beyond L~11 inward [Rymer et al., 2008].

The most well-established transport mechanism in this radial range is the centrifugally-driven interchange instability, which has been identified as an important process moving cold, inner-magnetosphere plasma outward and hot, outer-magnetosphere material inward to replace it. Numerous studies have examined the properties of discrete flux tubes or flow channels identified as the inflow elements of the interchange instability. In particular, the radial distribution of the occurrence of discrete interchange signatures indicates the depth in the magnetosphere to which interchange can deliver hot plasma [e.g., Hill et al., 2005; Chen and Hill, 2008; Kennelly et al., 2013]. Such discrete injections are common, but surveys have found that clear, distinct events are relatively infrequent, depending on the phenomenology used to identify them (~1/hour [Chen and Hill, 2008] to <1/day [Kennelly et al., 2013]). More often, the suprathermal electron population is more continuous in time and space. Nevertheless, it is generally thought [e.g., Rymer et al., 2008] that the suprathermal population in the inner magnetosphere is the product of many interchange events, delivering hot plasma that subsequently drifts and mixes azimuthally.

Figure 1a is an example of a rather typical inbound pass by the Cassini spacecraft through the inner magnetosphere on 13 Feb 2010. The figure shows the color-coded energy flux of electrons observed by the Electron Spectrometer (ELS), part of the Cassini Plasma Spectrometer (CAPS) [Young et al., 2004], for 10.5 hours as Cassini traveled from L~10 to L~4.6. Within this pass there are a few examples of discrete injections that show the characteristic energy dispersion analyzed by Hill et al. [2005] and Chen and Hill [2008] (point 1, marked below the time axis). There are also a few examples of the very recent injections described by Burch et al. [2005], which show little energy dispersion and are characterized by an absence of electrons at thermal energies (point 2, also marked below the time axis). In addition to those, there is a general suprathermal continuum, with temporal structure on the same scale as the identifiable injections.

In Figure 1a there is also a fairly sharp cutoff in the suprathermal population after ~0800 UT (L~7). This sharp drop in the intensity of the hot electrons has been noted previously [e.g., Rymer et al., 2007; Schippers et al., 2008]. Rymer et al. [2007] attributed it to enhanced losses (energy loss in collisions with neutrals and/or pitch-angle scattering into the atmospheric loss cone) at lower L values. However, they also mentioned that the inner edge of the hot electron population may be due to transport effects; they suggested that the observed energy dependence of this hot-electron cutoff [Rymer et al., 2007] may be due to the faster azimuthal drift out of the injected flux tubes by more-energetic particles [see also Burch et al., 2005; Paranicas et al., 2016].

Another noteworthy feature apparent in Figure 1a is seen beginning around 1140 UT, when the energy flux appears to increase uniformly across all energy channels above ~20 eV. Rather than true electron fluxes in the ELS energy range, this is the signature of background caused by penetrating radiation-belt particles, both electrons with energies above about 1 MeV and ions with energies of 10's of MeV. In the vast majority of Cassini's passes through the inner magnetosphere, there is a clear gap between the inner edge of the hot-electron population and the onset of significant penetrating background so that the presence of the background does not affect our ability to identify the inner edge. We will return to this point below.

A different pass through the inner magnetosphere is illustrated in Figure 1b. This pass, on 20 March 2010, occurred two orbits after the one shown in Figure 1a, under very similar orbital conditions. Both passes were at very low latitudes near midnight local time. It is clear, however, that the hot electron population in the second event extends much deeper into the inner magnetosphere, with the inner edge near L=5.2, compared to L~7 in Figure 1a. Moreover, the boundary is quite sharp, with very significant fluxes dropping sharply to near zero in a short distance. It is unlikely that the neutral gas in the inner magnetosphere has changed substantially between these two orbits, causing the electron loss region to contract. It is also unlikely that such a distributed loss region could produce a sudden sharp radial cutoff in the suprathermal population. Rather, we find it more plausible that the inward transport has varied, delivering the hot population deeper into the magnetosphere in the case of Figure 1b. In this interpretation, it is the transport itself that governs the location of the inner edge of the hot electron population, transport that may well vary temporally.

In this study, we explore the possibility that the inner edge of the hot-electron population is the result of the depth of penetration of the inward transport process. In particular, we examine the temporal and spatial variability of this cut-off L-shell, compare it with the radial range over which discrete interchange injections are observed, and explore its possible relationship to the radial extent of the radiation belts and to solar wind properties. We find clear evidence that the inner edge varies significantly with time: from orbit to orbit and even from inbound to outbound during a single pass through the inner region, and we discuss the implications of this variability.

2. Instrumentation and Analysis

We use data from the CAPS/ELS, as illustrated in Figure 1 [Coates et al., 1996; Linder et al., 1998; Young et al., 2004; Lewis et al., 2008]. Briefly, CAPS/ELS is a top-hat hemispherical electrostatic analyzer covering the energy range of 0.58-26,000 eV in 63 logarithmically spaced energy channels, with one energy sweep every 2 s. The analyzer comprises 8 anodes, each with an angular field of view (FOV) of 20˚x5˚. Because Cassini is a non-spinning spacecraft, the FOV is swept across the sky by the rotation of an actuator that can nominally scan ±104˚, providing coverage of 56% of the full 4π solid angle. Combined with simultaneous magnetometer measurements, it is thus possible for ELS to provide information about the nature of the electron pitch angle distribution. For the present study, however, we use fluxes averaged over all 8 detectors and over 16 consecutive energy sweeps, which comprise a so-called A-cycle of data, thus approximating an omnidirectional average.

From data files available from the Planetary Data System, we follow the prescription in Section 9.3.4 of the CAPS_PDS_USER_GUIDE [Wilson et al., 2012] to convert raw ELS counts C_{lmn} for each energy (l), azimuth (m), and polar angle (n) in a given A-cycle to number flux j_{lmn} using the expression

$$j_{lmn} = \frac{C_{lmn}}{S_n G_{ln} E_l \tau} \quad (1)$$

where C_{lmn} are the counts in a particular channel; S_n is a scale factor that depends on the anode and the microchannel-plate high voltage level; G_{ln} is the geometric factor (including the efficiency), which depends on the anode and the energy level; E_l is the energy; and τ is the accumulation time for a single measurement (0.0234375 s). The values of the various parameters in Equation 1 can be found in the CAPS_PDS_USER_GUIDE.

As mentioned above, the individual fluxes (Eq. 1) are then averaged over all anodes and all azimuths in an A-cycle to produce an A-cycle averaged flux spectrum which is then merged with ephemeris data and further averaged into L bins of width ΔL=0.1. A set of L bins between L=4 and L=12 is accumulated for each half-orbit (inbound or outbound) of Cassini data, providing a basic data set of bin-averaged fluxes in 80 L bins x 63 energies x 336 half-orbits, covering the intervals when CAPS was operating between Saturn Orbital Insertion (1 Jul 2004) and the last perigee pass before the end of CAPS data (20 May 2012).

For each half-orbit in this basic data set, we identify the innermost extent of the hot-electron population by setting a simple threshold condition for the flux at each energy level. We focus on energy levels 12, 18, and 24 (corresponding to electron energies of 5797 eV, 2054 eV, and 728 eV, respectively), which are representative of the suprathermal population and typically show clear flux enhancements when that population is present (c.f., Figure 1). Starting at a low L bin (described in the next paragraph) and working outward, we identify the first bin where the flux exceeds the threshold for that energy level.

To avoid false identifications of the inner hot-electron boundary caused by penetrating radiation, the region of significant background contamination must first be identified before the search for the inner edge of the hot electrons can be conducted. Thus, the first step in the search is to find the outermost L shell where the penetrating radiation has significant levels. To do this, we use the highest-energy ELS channel, which typically has very few ambient electrons deep in the magnetosphere (c.f., Figure 1) and for which the count rate is thus dominated by penetrating particles. Starting at the lowest L bin and working outward, we identify the first bin where the "flux" in this channel falls below a specified value. By trial and error, we find that an apparent flux of 100 $cm^{-2}\ s^{-1}\ sr^{-1}\ eV^{-1}$ provides a good determination of where the penetrating background becomes low enough to allow the suprathermal electrons to be seen, but the results from using 50 or 150 are essentially the same. The search for the inner edge of the hot electrons then begins from that L value and works its way outward.

Figure 2 shows the outer boundary of the penetrating radiation determined according to the foregoing procedure. The figure shows the color-coded apparent flux in energy channel 1, which at low L is actually dominated by the penetrating radiation (red colors). The blue line at low L is the location where this "flux" falls below the threshold of 100. It is apparent from Figure 2 that the intensity and extent of the penetrating background in ELS does vary with time, usually rather slowly but occasionally fairly sharply over just an orbit or so. In an analysis of the outer boundary of the >1 MeV electron radiation belt, Roussos et al. [2014] found similar and even greater variability. In the results and discussion sections below, the boundary identified by Roussos et al. will be compared with the ELS penetrating boundary determined here.

As mentioned above, the inner edge of the hot plasma population is identified using a simple threshold flux value for each energy channel. Because we are using 0.1 R_s bins for the identification, the process discriminates against isolated injections that are occasionally seen inward of the main hot population. Further, the location of the identified edge is weakly dependent on the threshold flux that is used. Varying the threshold provides a way of estimating the uncertainty in the determination. Figure 3 shows the results of applying three different thresholds to each of the three energy channels 24, 18, and 12 (5797 eV, 2054 eV, and 728 eV, respectively). Figure 3a shows the color-coded bin-averaged flux of electrons in channel 18, half-orbit by half-orbit, for the first 50 half-orbits of the mission (1 July 2004 – 29 Apr 2006). Superimposed are the outer edge of the penetrating background, as described above, and the inner edge of the 2054 eV population, for a threshold flux value of 37 $cm^{-2}\ s^{-1}\ sr^{-1}\ eV^{-1}$. Figure 3b shows the color-coded inner edge derived for all three energy channels, offset slightly in half-orbit number for clarity. The solid dots show the inner edge determined from the center value of the three thresholds used, and the error bars show the range of edge determinations associated with the lower and upper threshold employed. The nine different thresholds are listed in Table 1.

Figure 3a reveals that the inner edge of the hot-electron fluxes is readily discernible and quite variable from orbit to orbit. Further, the simple threshold requirement apparently does a good job of identifying the inner edge, except where ELS coverage does not extend inside of L=5.6, in which case we do not report an edge location.

Figure 3b shows that varying the threshold does at times result in an uncertainty in the derived edge value by 1 R_s or more, with lower thresholds resulting in lower edge values. However, for most of the points the determination is well localized. The variability in the determination over these 50 orbits is substantially greater than the typical uncertainty in the measurements. For the full data set, the median differences between the edge determined with the medium threshold and those determined by either the high or low thresholds are <0.2 R_s for all three energy levels, and the average difference is <0.5 R_s.

Figure 3b also indicates that the edges determined on the basis of the three different energy channels typically agree quite well with each other, especially when the uncertainty in the determinations is low. This is partly due to the fact that we have chosen the three thresholds for each channel such that over the entire data set the median edge values for the low, medium, and high thresholds are statistically the same for the three energy levels. But the point-to-point tracking of the three channels seen in Figure 3b shows that within this constraint, the determinations using those three channels do agree quite well.

The horizontal bars in the two panels of Figure 1 show the ranges of the edges that were determined for these specific passes, based on the thresholds in Table 1, and the vertical dashed lines indicate the centroid of values obtained from the medium threshold for all three channels. The dependence on the threshold is apparent, but the medium threshold values do seem to identify the inner edge quite well.

Of the 336 half-orbits executed by Cassini between 1 Jul 2004 and 20 May 2012, the above procedure identified (225, 218, 212) inner edge values for Channel 12, (226, 219, 215) for Channel 18, and (227, 222, 212) for Channel 24, where the three values in each set correspond to the low, medium, and high threshold values listed in Table 1. Most of the half-orbits for which an edge was not determined corresponded to times when CAPS was off or not taking data inside of L=5.6. A few edges were not identified because the thresholds were too high (as shown by the fact that successively higher thresholds result in successively fewer determinations).

3. Results

Figure 4 is a statistical comparison of the outer edge of the penetrating background derived from ELS data as described above and the outer edge of the >1 MeV electron radiation belt determined by Roussos et al. [2014]. The principal difference between them is that the outer boundary found by Roussos et al. is typically ~2 R_s further from Saturn than is the point where the ELS penetrating background falls below the threshold we have stipulated. This is presumably just due to a different flux threshold being adopted in the two studies; the MIMI instrument used by Roussos et al. is designed to measure energetic particles and is thus more sensitive to them than is ELS.

Figure 5 shows a point-by-point comparison of the ELS-derived background edge with the radiation belt boundary found by Roussos et al. [2014] for the years 2005 through 2010. To account for the different sensitivity of the two instruments, we have simply offset the L range of the two measurements by 2 R_s. The Roussos data are plotted in blue according to the left-hand axis, while the ELS boundary is plotted in red according to the right-hand axis. With the offset, it is easier to compare the temporal variations of the two determinations.

While one could argue that some intervals in Figure 5 show similar trends in the two derived outer boundaries, a detailed correspondence is far from obvious. Both show evidence of variability from orbit to orbit, and the variability is generally greater in the >1 MeV electron boundary than in the ELS background (see also Figure 4). Nevertheless, we find a weak correlation (R=0.315) between the two boundary determinations, which for the 230 points in our analysis has a probability of only 10^{-6} of being random. We return to this comparison in the discussion below.

In Figure 6 we turn to our primary objective, the inner edge of the hot-electron population. That figure shows the inner edge determined using the medium thresholds (Table 1) for all three energy channels (12, 18, 24), as described above, for the entire data set. Figure 7 shows the statistics of the boundary determinations for all three thresholds, for all three energy levels. From both Figures 6 and 7 it is apparent that there is large variability in the depth of penetration of the hot electrons. At the medium thresholds, ~90% of the inner boundaries of hot-electron penetration lie between L~4.7 and 8.4, with a median near 6.2.

Figure 6 shows that the variability is rapid, from orbit to orbit and even from inbound to outbound on the same orbit. Figure 8 explores this variability in greater detail. Shown there are distributions of values of ΔL, where ΔL is the difference in inner edge determinations between each inbound pass and the subsequent outbound pass (blue); between subsequent inbound passes (red); and between subsequent outbound passes (green) for the entire data set. We have used the edge determinations from Channel 18, with the medium threshold from Table 1. Superimposed on these distributions, in light dashed lines, are several distributions derived by taking the observed set of edge values and reordering it randomly before calculating the difference between two consecutive values. If there were persistence in the edge values from pass to pass, one would expect the distribution of ΔL values to be narrower than for a random arrangement of the values. Figure 8 shows that the distributions of observed pass-to-pass changes are only slightly narrower than the reordered distributions, if at all. Thus, while there may be some very weak repeatability in the observed inner edge, each observed value is largely unrelated to the previous value. This contrasts with the situation found for the outer boundary of the radiation-belt electrons, which shows clear temporal persistence on the timescale of inbound to outbound passes [Fig. 9b of Roussos et al., 2014].

It has been noted previously [DeJong et al., 2010] that the flux of electrons in the energy range 12-100 eV is enhanced in the presence of hot, injected electrons and that this flux enhancement extends inward closer to Saturn on the night side than on the day side. One might thus expect a day-night asymmetry in the properties of the hot electrons as well. Figure 9 shows a sequence of energy-time spectrograms of ELS energy flux for all the passages through the inner magnetosphere during 2010, during which time the inbound passes all occurred between LT~22 and LT~3, whereas the outbound passes all occurred between LT~10 and LT~16. For each passage through the inner region ($4.5<L<10$), two spectrograms are shown: The upper one in each set is the inbound (nightside) pass, and the lower one is the outbound (dayside) pass. The inbound passes are all time-reversed so that L increases from right to left for both passes, enabling more direct inbound/outbound comparisons.

In Figure 9, the variability in the depth of penetration of hot electrons emphasized above is clearly visible. There are major differences from orbit to orbit and from inbound to outbound, which are separated by only ~10-20 hours. Moreover, there does appear to be a day/night difference in the appearance of the hot-electron population, with the nightside population often more robust than the dayside one. Indeed, there are a few passes (e.g., 13-14 Aug) where the dayside hot electrons seem almost entirely absent.

Figure 10 shows the inner edge determinations from Channel 18 with the medium threshold for all of the inbound and outbound passes in 2010. While there are several exceptions, the inner edge on the outbound (dayside pass) does typically seem to be further from Saturn than on the inbound (nightside). The three dashed vertical lines indicate passes where the dayside fluxes were so low that no inner edge was found.

To explore further a possible local time dependence of the depth of penetration of the hot electrons, Figure 11 shows, for four different local time ranges, the occurrence distribution of the inner edge of the Channel 18 electron fluxes, determined using the medium threshold of Table 2. The large majority of determinations in our data set fall in the nightside range (21-03 LT), so the distributions for the other LT ranges do not have good statistics, but it does appear that there is a significant difference in the typical locations of the inner edge on the dayside compared to the night side. Relative to the night side, there are substantially more dayside boundaries at larger L values and many fewer in the range $5<L<7$. There are too few measurements in the dawn and dusk sectors to draw conclusions for those.

Finally, we wish to examine the possibility that conditions in the solar wind have some control over the depth of penetration of the hot electrons into Saturn's inner magnetosphere. At the Earth, it is well known that solar wind properties (especially the north-south component of the interplanetary magnetic field and the solar wind velocity) affect the strength of the convection that brings plasma-sheet material in close to the Earth. At Saturn there is now evidence that under conditions of high solar wind dynamic pressure the solar wind may have an important influence on magnetotail dynamics [Thomsen et al., 2015], which may control the injection of outer-magnetosphere material into the inner region.

At Saturn, of course, there is no upstream solar wind monitor to show exactly what the input conditions are to the magnetosphere, but we can estimate the upstream solar wind plasma properties with the University of Michigan mSWIM 1.5-D MHD model, with solar wind conditions as observed at 1 AU as a boundary condition [Zieger and Hansen, 2008]. The mSWIM predictions of solar wind properties are publicly available on the University of Michigan web site (http://mswim.engin.umich.edu/). Although the model does not reliably predict the magnetic field orientation, it has been shown to do a reasonably good job of estimating the solar wind density and flow speed, with a fidelity that depends on the relative alignment of Earth and Saturn and on the nature of the solar wind environment [see Zieger and Hansen, 2008, for details]. Figure 12 shows 100 days of mSWIM predictions at Saturn (from 21 Sep 2007 to 31 Dec 2007) compared with ELS determinations of the penetration distance of the hot electrons. The top two panels show the modeled solar wind speed and dynamic pressure and illustrate well the recurrent stream structure that characterized the solar wind at Saturn during this phase of the solar cycle. The stippled regions indicate Cassini periapsis passes, and the bottom panel shows the inner electron boundary for the three energy channels (12, 18, and 24), determined using the medium flux thresholds in Table 1, with the error bars giving the range that results from using the low and high thresholds.

The first three periapsis passes in Figure 12 occurred during the declining phase of solar wind speed enhancements, in regions of low dynamic pressure. The fourth periapsis pass occurred during a period when the dynamic pressure was almost two orders of magnitude higher than in the earlier low-dynamic-pressure intervals. The fifth periapsis pass occurred during a transition from low to high dynamic pressure. In spite of the large difference in ambient dynamic pressure during these periapsis passes, there is no clearly discernible difference in the penetration distance of the hot electrons. The inner boundary during the high dynamic-pressure interval is not particularly higher or lower than in the previous low dynamic-pressure intervals.

In Figure 13, the relationship between the penetration distance for Channel 18 (medium threshold) and the solar wind speed and dynamic pressure is examined for the entire date set. Each data point shows the mSWIM-predicted Vsw or Pd at the time of the periapsis pass, with error bars showing the range of estimated values during the preceding and following 24 hours. The two left-hand panels show the results for the full data set, and the right-hand panels show only the upper and lower quartiles of the solar wind parameters. It is clear from this figure that the range of penetration L values is basically independent of the solar wind speed and dynamic pressure.

4. Discussion

For most Cassini passes through the inner magnetosphere of Saturn, the hot-electron population largely disappears inside of some cut-off L-shell. The cut-off L-shell is quite variable from pass to pass, but it typically lies outside (at larger L than) the region of penetrating background in ELS, enabling our simple threshold-based algorithm to identify the hot-electron cutoff distance in each pass.

The outer edge of the penetrating background in ELS generally lies ~2 R_s inward of what Roussos et al. [2014] have identified as the outer boundary of the >1 MeV electron population, and their boundary exhibits greater variability than ours. There are times when the excursions in the two boundaries appear to track each other, at least in the sign of the change, but many other times when they do not. It is worth noting that the ELS penetrating background is produced by a combination of energetic electrons (>1 MeV) and trapped protons (probably >several 10s of MeV). Studies of data from the Cassini MIMI instrument have shown that the proton radiation belt is rather stable, whereas the electron belt is more variable [Roussos et al., 2011, 2014, and references therein]. The proton belt extends out to L~5 and may thus be dominating the penetrating background in ELS much of the time, with radiation-belt electrons contributing the small element of variability to the background. The relative contribution of energetic protons and energetic electrons to the ELS background is beyond the scope of the present study, and the important fact for our current purposes is that the background does not prevent us from identifying the inner edge of the hot-electron penetration.

In identifying the inner boundary of the hot electrons, we have used a simple fixed threshold for each energy channel. We have made no attempt to correct the fluxes for the latitude of the spacecraft at each measurement point as was done by Roussos et al. [2014]. The main reason is that, unlike the high-energy radiation belt particles studied by Roussos et al., the pitch-angle distributions of hot electrons are not always peaked in the perpendicular direction [e.g., Schippers et al., 2008; Rymer et al., 2007; Clark et al., 2014], so a universal correction factor is not applicable and might even be counter-productive in times of non-pancake distributions. Rymer et al. [2007] argued that the observed pitch-angle distributions in the CAPS energy range suggested efficient pitch-angle scattering. At higher E (>20 keV) Clark found ~80% pancake, but still rather flat. Therefore, we expect a rather weak latitude dependence of the fluxes, and for simplicity we have adopted a single threshold. In practice, for some high-latitude passes we do see lower fluxes, which in some cases never exceed our threshold, so no cutoff L is found. However, the statistics for 2008 (high latitude) vs 2005 and 2010 (low latitude) do not show any systematic offsets.

At higher electron energies, in the MIMI range, Rymer et al. [2007] found a clear energy dependence to the radial location of the sharp drop-off of the phase space density at low L values, with higher energies having a drop-off at higher L values. They hypothesized that this is due either to precipitation losses in the inner region (strong pitch angle scattering is faster for higher-energy particles) or to the tendency for more-energetic particles to gradient-drift out of an injection channel before it reaches its innermost extent [see also Paranicas et al., 2016]. At the ELS energies we have studied, this energy dependence is likely to be quite weak and in fact is not apparent in our results.

In general, all three energy levels show similar trends from pass to pass. As might be expected, the derived boundary locations do depend somewhat on the exact value of the threshold flux that is used in the analysis (Table 1), but again the trends are similar, and we have used the variation with respect to the threshold value as a measure of the uncertainty in the derived boundary location.

At the medium thresholds for all three channels, 90% of the inner boundary values lie between L~4.7 and 8.4, with a median near L=6.2. The depth of penetration of hot electrons is therefore consistent with the range of L values over which discrete interchange injections have been observed [e.g., Hill et al., 2005; Chen and Hill, 2008; Kennelly et al., 2013], strengthening the case that the interchange process is responsible for delivering the bulk of the hot electrons seen in the inner magnetosphere.

The penetration distance can vary dramatically from pass to pass, including between inbound and outbound passes on the same orbit (with a time separation of ~10-20 hours). Unlike the outer boundary of the radiation-belt electrons determined by Roussos et al. [2014], there is no more coherence between subsequent passes (inbound to outbound, inbound to inbound, outbound to outbound) than between a random sampling of passes. Thus, the penetration distance apparently changes on time scales too short for Cassini to measure (<~ few hours). We suggest that these time scales may reflect the time between successive bursts of interchange motions, perhaps triggered by tail reconnection episodes as Saturn sheds internally produced plasma down the tail and into the solar wind.

Most of our determinations are from the midnight quadrant, where the occurrence clearly peaks near L~5.5-6. In other local time sectors, the occurrence distribution is broader, and especially in the noon quadrant there is a significantly higher percentage of boundaries found between L~7.5 and 9.5 (Figure 11). For the low-latitude passes of 2010, which were inbound near midnight local time and outbound near noon, most of the midnight passes show deeper penetration than the noon passes (Figure 10). A night-to-day outward radial displacement ~0.2-1 R_s might be expected in the L range ~5-6 due to the existence of the noon-to-midnight electric field inferred to exist within the inner magnetosphere [c.f., Thomsen et al., 2012; Wilson et al., 2013; and references therein], but the occurrence distributions in Figure 11 do not exhibit a straightforward outward shift from midnight to noon. Indeed, there remain numerous dayside passes where the boundary is found at values as low as L~4.5-5. Interestingly, Figures 13 and 14 of Thomsen et al. [2012] suggest that outward displacements associated with the noon-to-midnight electric field may be greatly diminished inside of L~5, so that penetrations to very low L values may not be much displaced during drift to the opposite local time sector, potentially accounting for the two-peaked distribution seen in Figure 11.

As seen in Figure 9, there also appears to be a day/night difference in the appearance of the hot-electron population, with the nightside population often more robust than the dayside one. This is in agreement with previous analyses [e.g., DeJong et al., 2010] and may suggest that the initial hot-plasma injections occur dominantly on the night side, gradually decaying as they are carried around to the dayside. However, there remains a lack of consensus regarding the local time of origin of discrete injection events [e.g., Chen and Hill, 2008; Kennelly et al., 2013], particularly since such studies have so far not taken into account the radial transport times of the injections [Paranicas et al., 2016]. This question merits further study.

Using mSWIM predictions to estimate the solar wind properties, we find that during several episodes of fairly prolonged (~10-15 d) low or high solar-wind pressure, there was no clearly discernible difference in the penetration distance of the hot electrons. The inner boundary during the high dynamic-pressure interval was not particularly higher or lower than in the previous low dynamic-pressure intervals, suggesting no strong dependence on what the solar wind was doing. Within a +/- 1d arrival window, there is no detectable correlation between the penetration distance and solar wind speed or dynamic pressure. It thus appears that internal dynamics such as the release of mass-loaded flux tubes are more likely responsible than solar wind variations in determining how deep in the magnetosphere hot plasma will be injected.

5. Conclusions

We have used anode-and-actuation-angle averages of hot-electron fluxes observed by CAPS/ELS and binned into 0.1- R_s bins in dipole L to explore the inner edge of the hot-electron population in Saturn's inner magnetosphere. The inner edge is almost always outside the region of strong penetrating background in the ELS detector, so we are able to determine the edge for most of Cassini's passes through the inner magnetosphere.

At energies of 5797 eV, 2054 eV, and 728 eV, 90% of the inner boundary values lie between L~4.7 and 8.4, with a median near L=6.2, consistent with the range of L values over which discrete interchange injections have been observed [e.g., Hill et al., 2005; Chen and Hill, 2008; Kennelly et al., 2013], and thus strengthening the case that the interchange process is responsible for delivering the bulk of the hot electrons seen in the inner magnetosphere. The occurrence distribution of the inner boundary is more sharply peaked on the night side than at other local times, perhaps as a consequence of the noon-to-midnight global electric field that exists within the inner magnetosphere.

The strong pass-to-pass variability in the hot-electron boundary may reflect a relatively short time between successive bursts of interchange motions, perhaps triggered by tail reconnection episodes as Saturn sheds internally produced plasma down the tail. There is no apparent dependence of the depth of penetration on large-scale solar wind properties, further supporting the likelihood that internal processes (magnetic stress on mass-loaded flux tubes) are dominating the injection of hot electrons into the inner magnetosphere.

Acknowledgements

This work benefited greatly from discussions held during two meetings of the International Space Science Institute (ISSI) team on "Modes of Radial Transport in Magnetospheres." Work at PSI was supported by the NASA Cassini program through JPL contract 1243218 with Southwest Research Institute. The Cassini project is managed by the Jet Propulsion Laboratory for NASA. MFT is grateful to Los Alamos National Laboratory for the support provided her as a guest scientist. All ELS data used for this study are available from the Planetary Data System (http://pds.nasa.gov/).

References

Burch, J. L., J. Goldstein, T. W. Hill, D. T. Young, F. J. Crary, A. J. Coates, N. André, W. S. Kurth, and E. C. Sittler Jr. (2005), Properties of local plasma injections in Saturn's magnetosphere, *Geophys. Res. Lett., 32*, L14S02, doi:10.1029/2005GL022611.

Chen, Y., and T. W. Hill (2008), Statistical analysis of injection/dispersion events in Saturn's inner magnetosphere, *J. Geophys. Res., 113*, A07215, doi:10.1029/2008JA013166.

Clark, G., et al. (2014), Evolution of electron pitch angle distributions across Saturn's middle magnetospheric region from MIMI/LEMMS, *Planet. Space Sci., 104,* 18, doi:10.1016/j.pss.2014.07.004.

Coates, A.J., C. Alsop, A.J. Coker, D.R. Linder, A.J. Johnstone, R.D. Woodliffe, M. Grande, A. Preece, S. Burge, and D.S. Hall, (1996), The electron spectrometer for the Cassini spacecraft. *J. British Interplanetary Soc. 45* (9).

DeJong, A. D., J. L. Burch, J. Goldstein, A. J. Coates, and D. T. Young (2010), Low-energy electrons in Saturn's inner magnetosphere and their role in interchange injections, *J. Geophys. Res., 115*, A10229, doi:10.1029/2010JA015510.

Hill, T. W., A. M. Rymer, J. L. Burch, F. J. Crary, D. T. Young, M. F. Thomsen, D. Delapp, N. André, A. J. Coates, and G. R. Lewis (2005), Evidence for rotationally driven plasma transport in Saturn's magnetosphere, *Geophys. Res. Lett., 32*, L14S10, doi:10.1029/2005GL022620.

Kennelly, T. J., J. S. Leisner, G. B. Hospodarsky, and D. A. Gurnett (2013), Ordering of injection events within Saturnian SLS longitude and local time, *J. Geophys. Res., 118*, 832–838, doi:10.1002/jgra.50152.

Lewis, G. R., et al. (2008), Derivation of density and temperature from the Cassini-Huygens CAPS Electron Spectrometer, *Planet. Space Sci., 56,* 901.

Linder, D.R., A.J. Coates, R.D. Woodliffe, C. Alsop, A.D. Johnstone, M. Grande, A. Preece, B. Narheim, and D.T. Young (1998), The Cassini CAPS Electron Spectrometer, *Measurement Techniques in Space Plasmas: Particles,* Geophysical Monograph, vol. 102, American Geophysical Union, pp. 257–262.

Paranicas, C., et al. (2016), Effects of radial motion on interchange injections at Saturn, *Icarus, 264,* 342, doi:10.1016/j.icarus.2015.10.002.

Roussos, E., N. Krupp, C. P. Paranicas, P. Kollmann, D. G. Mitchell, S. M. Krimigis, T. P. Armstrong, D. R. Went, M. K. Dougherty, and G. H. Jones (2011), Long- and short-term variability of Saturn's ionic radiation belts, *J. Geophys. Res., 116*, A02217, doi:10.1029/2010JA015954.

Roussos, E., et al. (2014), The variable extension of Saturn's electron radiation belts, *Planet. Space Sci., 104,* 3, doi:10.1016/j.pss.2014.03.021.

Rymer, A. M., et al. (2007), Electron sources in Saturn's magnetosphere, *J. Geophys. Res., 112,* A02201, doi:10.1029/2006JA012017.

Rymer, A. M., B. H. Mauk, T. W. Hill, C. Paranicas, D. G. Mitchell, A. J. Coates, and D. T. Young (2008), Electron circulation in Saturn's magnetosphere, *J. Geophys. Res., 113*, A01201, doi:10.1029/2007JA012589.

Schippers, P., et al. (2008), Multi-instrument analysis of electron populations in Saturn's magnetosphere, *J. Geophys. Res., 113*, A07208, doi:10.1029/2008JA013098.

Wilson, R. J., F. Crary, L. K. Gilbert, D. B. Reisenfeld, J. T. Steinberg, and R. Livi (2012), Cassini Plasma Spectrometer (CAPS) PDS User's Guide, available electronically at http://ppi.pds.nasa.gov/search/view/?f=yes&id=pds://PPI/CO-E_J_S_SW-CAPS-2-UNCALIBRATED-V1.0/DOCUMENT/CAPS_USER_GUIDE/CAPS_PDS_USER_GUIDE_V1_00&o=1.

Thomsen, M. F., C. M. Jackman, D. G. Mitchell, G. Hospodarsky, W. S. Kurth, and K. C. Hansen (2015), Sustained lobe reconnection in Saturn's magnetotail, *J. Geophys. Res., 120*, 10,257–10,274, doi:10.1002/2015JA021768.

Young, D. T., et al. (2004), Cassini Plasma Spectrometer investigation, *Space Sci. Rev., 114*, 1–112.

Zieger, B., and K. C. Hansen (2008), Statistical validation of a solar wind propagation model from 1 to 10 AU, *J. Geophys. Res., 113,* A08107, doi:10.1029/2008JA013046.

Table 1. Adopted Flux Threshold Values ($cm^{-2}\ s^{-1}\ sr^{-1}\ eV^{-1}$)

	Channel 12 (5797 eV)	Channel 18 (2054 eV)	Channel 24 (728 eV)
Low	14	21	27
Medium	25	37	50
High	40	60	90

Figures

Figure 1. Color-coded electron count rate (proportional to energy flux) as a function of energy and time for intervals on a) 13 February 2010 and b) 20 March 2010. As Cassini moves inward toward Saturn, the intensity of the hot electron population (>100 eV) drops sharply at an inner boundary marked by the dashed vertical lines. The horizontal lines show the range of boundary locations at three different energy levels, identified based on the flux thresholds in Table 1. Points 1 and 2 marked below the time axis in a) indicate times when dispersed and undispersed, respectively, discrete injections can be seen.

Figure 2. Apparent number flux in ELS energy channel 1 (nominally 26 keV) as a function of L and half-orbit number for all CAPS data (1 July 2004 – 20 May 2012). The intense "fluxes" at low L values are actually due to penetrating particles from Saturn's radiation belts. The blue line at low L is the location where the apparent flux falls below 100 cm^{-2} s^{-1} sr^{-1} eV^{-1} and identifies the outer boundary of the penetrating background region.

Figure 3. a) Fluxes of electrons at 2054 eV, averaged over ELS anode and all azimuths in an A-cycle, and binned in 0.1- R_s bins for each half-orbit. Bin-averaged fluxes are shown as a function of L and half-orbit number for the first 50 Cassini half-orbits (1 July 2004 – 29 Apr 2006). The blue line at low L values is the identified outer boundary of the penetrating background, and the stars at higher L are the identified inner boundary of the hot electrons, based on the medium threshold for channel 18 in Table 1. b) Identified

inner boundary of the hot electrons at three different energy channels, for the same 50 half-orbits as panel a. Symbols show the values determined using the medium thresholds in Table 1, and the error bars show the range of values if the low and high thresholds are used.

Figure 4. Occurrence statistics of the outer edge of the ELS penetrating background (left) and the >1MeV electron radiation belts (right) [Roussos et al., 2014]. The upper and lower boundaries of the bars correspond to the 5^{th} and 95^{th} percentile levels, while the dashed horizontal lines show the 25^{th} and 75^{th} percentiles, and the solid horizontal bars indicate the median values.

Figure 5. Point-by-point comparison of the outer edge of the ELS penetrating background (red, right-hand axis) and the outer edge of the >1MeV electron radiation belts (blue, left-hand axis) [Roussos et al., 2014]. The ELS boundaries are offset by 2 R_s to facilitate comparison of the two.

Figure 6. L value of the inner edge of the hot-electron population determined using the medium flux thresholds (Table 1) for three ELS channels.

Figure 7. Occurrence statistics of the inner edge of the hot-electron population derived for three different energy channels, with three different flux thresholds for each (Table 1). The flux thresholds are chosen to yield the same median values for all three channels. The upper and lower boundaries of the bars correspond to the 5^{th} and 95^{th} percentile

levels; the dashed horizontal lines show the 25th and 75th percentiles; and the solid horizontal bars indicate the median values.

Figure 8. Occurrence distributions of the change in inner boundary location from each inbound pass to the subsequent outbound pass (blue), from each inbound pass to the subsequent inbound pass (red), and from each outbound pass to the subsequent outbound pass (green). The black dashed curves show the occurrence distribution from pass to pass when the various passes are reordered randomly. Different curves result from different randomizations.

Figure 9. Electron energy-flux spectrograms for fifteen passes through the low-latitude inner magnetosphere in 2010. For each orbit there are two panels: The upper corresponds to the inbound pass (reversed in time so that L increases to the right), and the lower corresponds to the outbound pass. Inbound passes all occurred on the night side (22<LT<3), and outbound passes all occurred on the day side (10<LT<16).

Figure 10. Comparison of the inner edge of the Channel 18 electron fluxes (medium threshold) for inbound (solid circles) and outbound (open circles) passes on the same orbits during 2010. Vertical dashed lines show orbits where the outbound fluxes were too low to allow the identification of the inner edge.

Figure 11. Occurrence distribution of the inner edge of the Channel 18 electron fluxes (medium threshold) for four different local time sectors.

Figure 12. Solar wind speed and dynamic pressure predicted for Saturn by the mSWIM 1.5-D MHD model for the interval from 21 September 2007 to 30 December 2007, a period when there were alternating intervals of sustained high and low dynamic pressure. The bottom panel shows the inner boundary of hot electrons for the three energy channels (12, 18, 24), with the stippled regions drawn to aid the comparison. In the bottom panel the open circles show the penetration distance derived with the medium threshold for each channel, and the error bars show the ranges between the low and high threshold values.

Figure 13. Solar wind speed (top row) and dynamic pressure (bottom row) calculated from the mSWIM model, versus the corresponding inner edge of the Channel 18 electron fluxes (medium threshold) for all data (left column) and for just the upper and lower quartiles of the solar wind parameters (right column). The error bars show the range of solar wind values predicted within ±1 day of the inner edge determination.

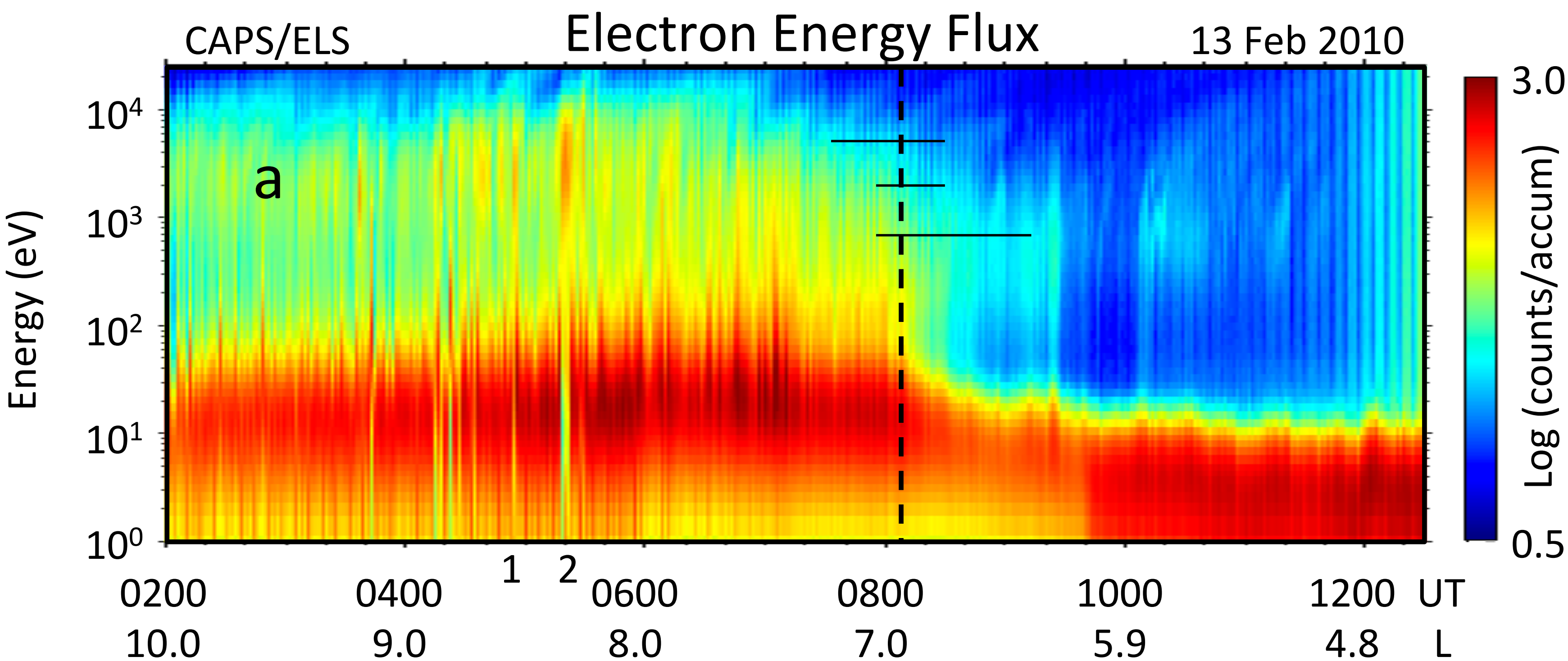
CAPS/ELS
Electron Energy Flux
13 Feb 2010
a
Energy (eV)
10^4
10^3
10^2
10^1
10^0
3.0
Log (counts/accum)
0.5
1
2
0200
0400
0600
0800
1000
1200
UT
10.0
9.0
8.0
7.0
5.9
4.8
L

Figure 1a.

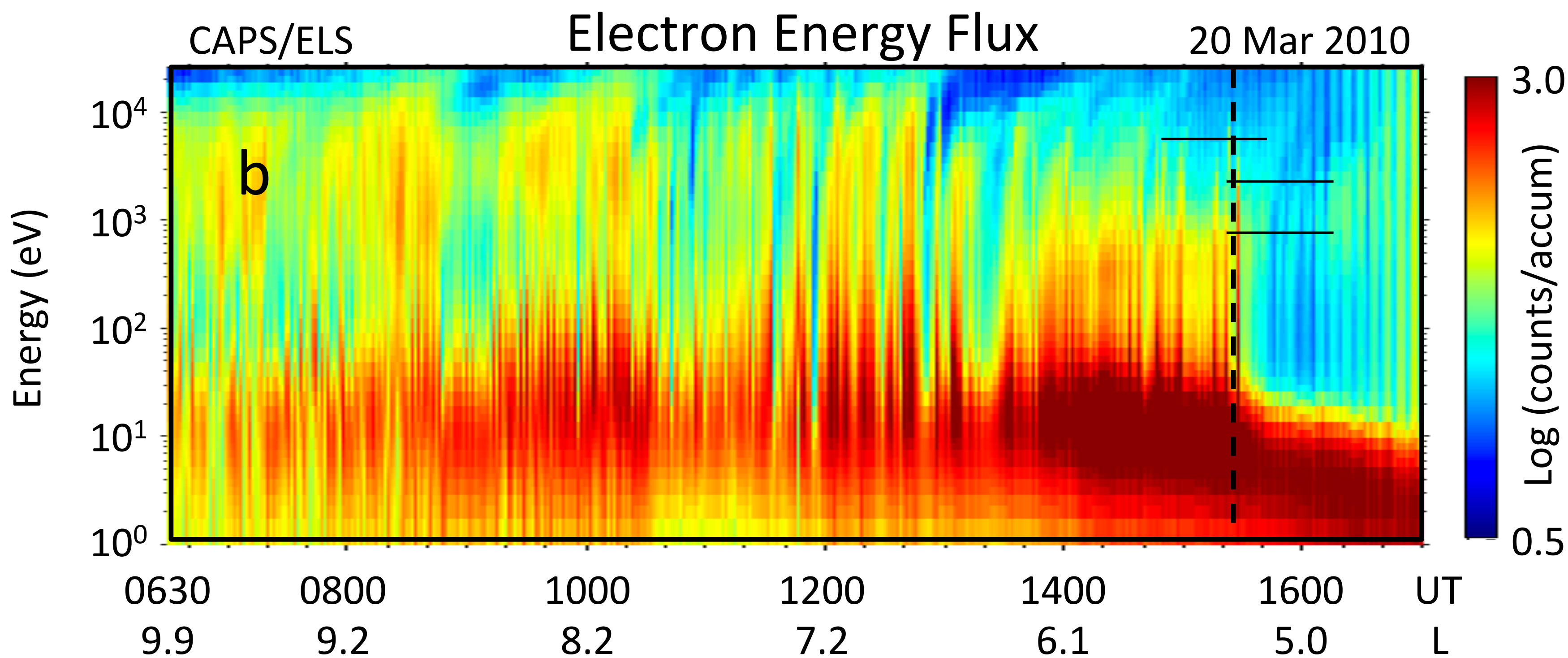
Electron Energy Flux
CAPS/ELS
20 Mar 2010
b
Energy (eV)
10^4
10^3
10^2
10^1
10^0
0630
0800
1000
1200
1400
1600
UT
9.9
9.2
8.2
7.2
6.1
5.0
L
3.0
0.5
Log (counts/accum)

Figure 1b.

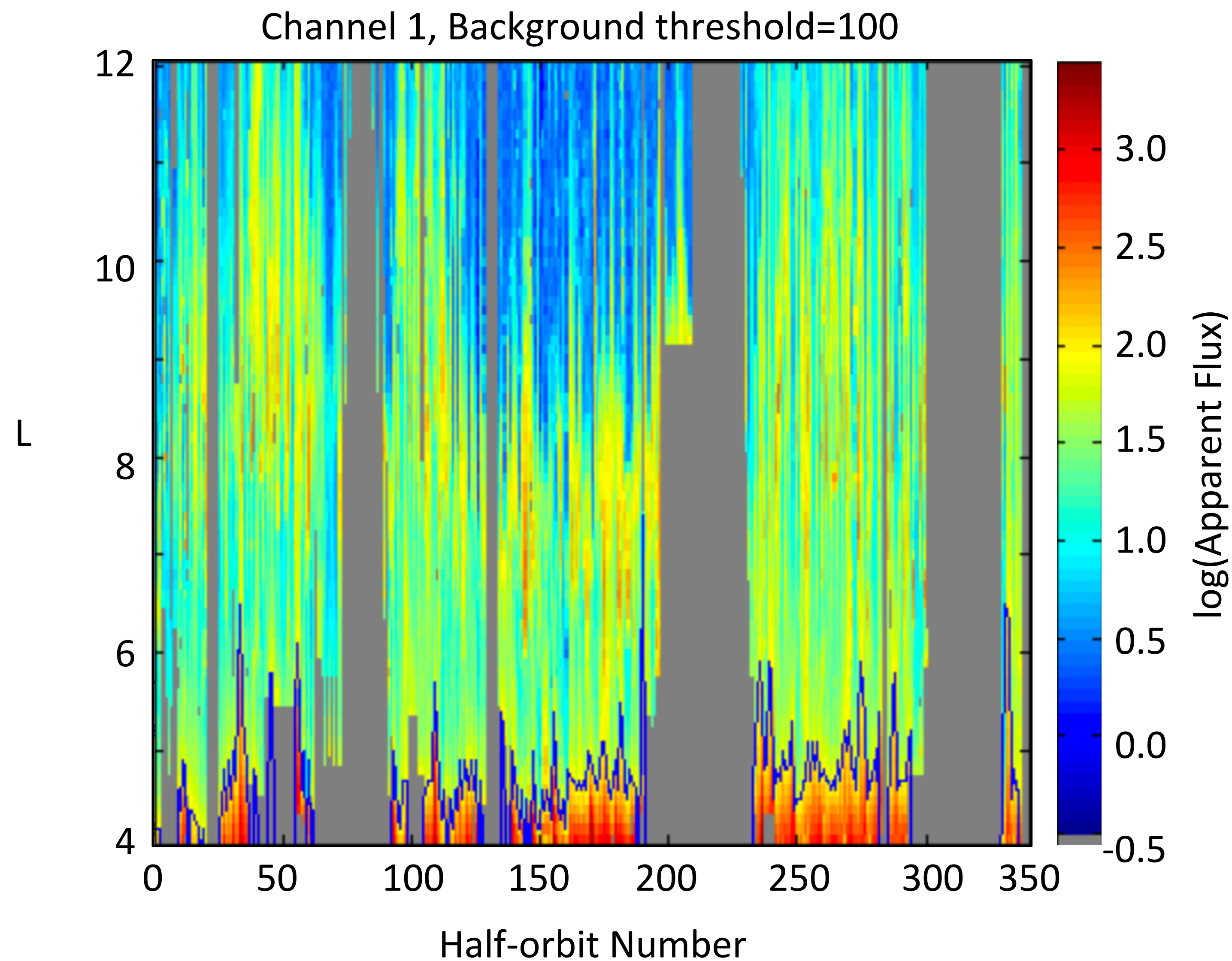

Channel 1, Background threshold=100
12
10
8
6
4
L
0
50
100
150
200
250
300
350
Half-orbit Number
3.0
2.5
2.0
1.5
1.0
0.5
0.0
-0.5
log(Apparent Flux)

Figure 2.

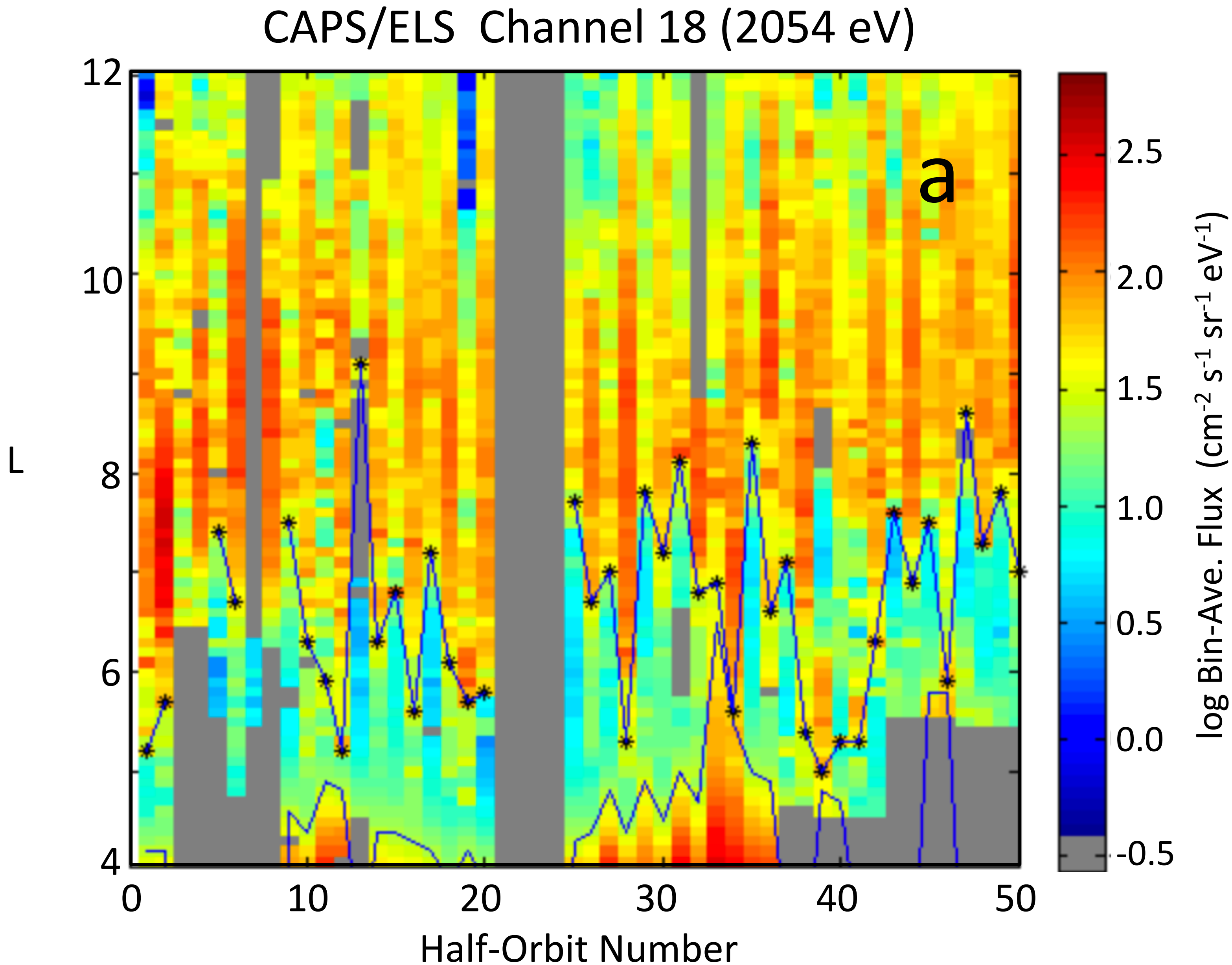
CAPS/ELS Channel 18 (2054 eV)
a
L
12
10
8
6
4
0
10
20
30
40
50
Half-Orbit Number
log Bin-Ave. Flux (cm^{-2} s^{-1} sr^{-1} eV^{-1})
2.5
2.0
1.5
1.0
0.5
0.0
-0.5

Figure 3a.

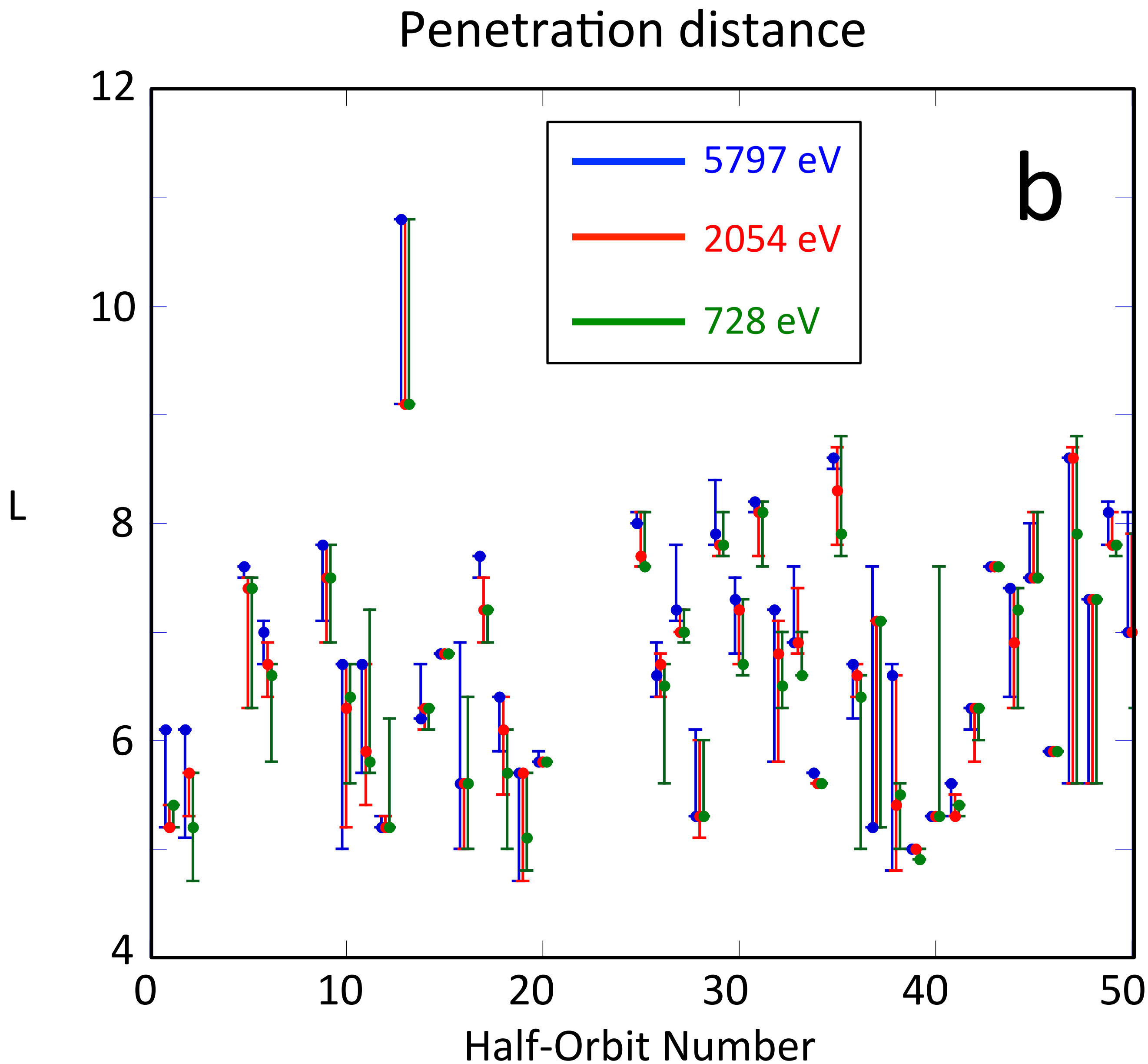

Penetration distance
12
10
8
6
4
L
0
10
20
30
40
50
Half-Orbit Number
5797 eV
2054 eV
728 eV
b

Figure 3b.

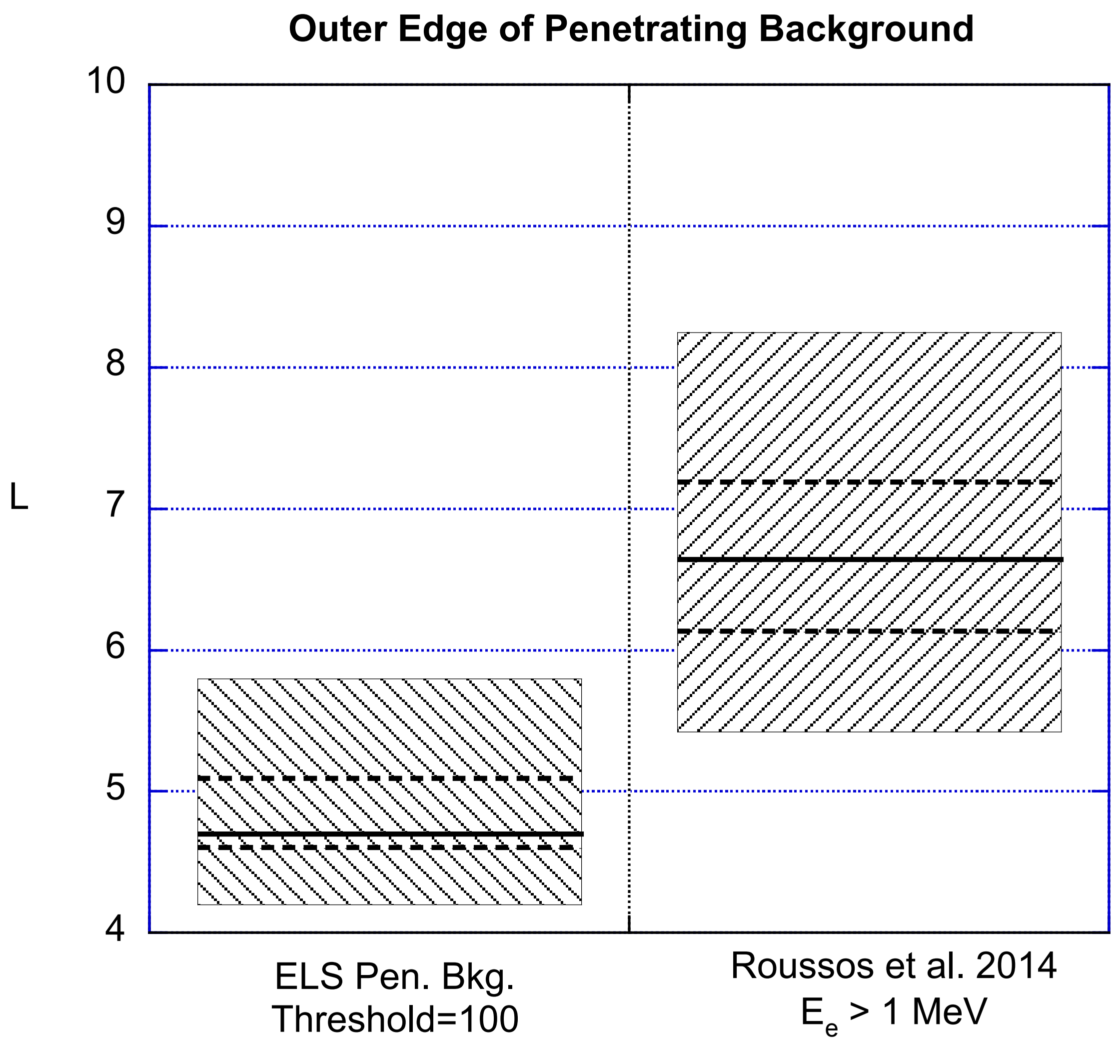
Outer Edge of Penetrating Background
10
9
8
7
6
5
4
L
ELS Pen. Bkg.
Threshold=100
Roussos et al. 2014
E_e > 1 MeV

Figure 4.

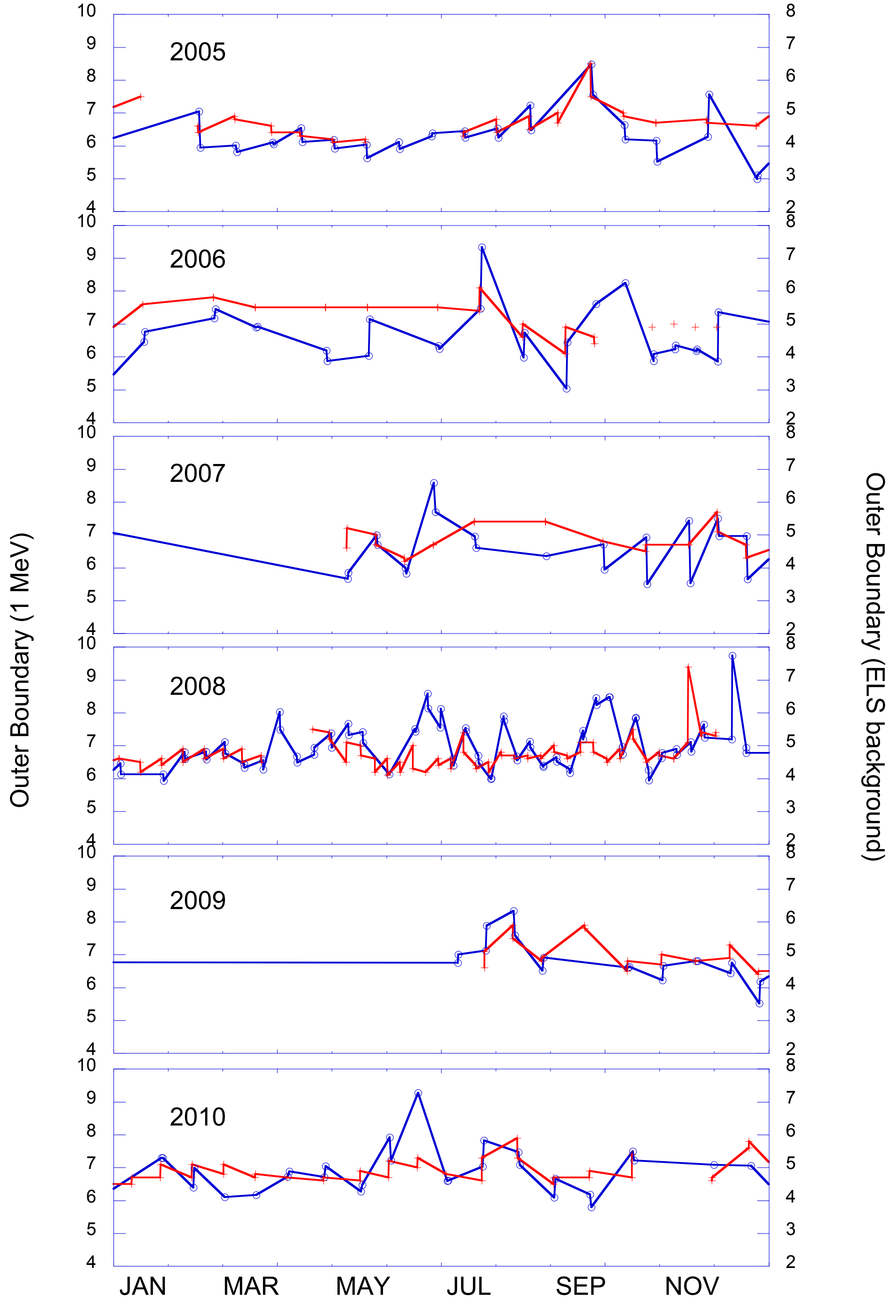
Outer Boundary (1 MeV)
Outer Boundary (ELS background)
2005
2006
2007
2008
2009
2010
JAN
MAR
MAY
JUL
SEP
NOV

Figure 5.

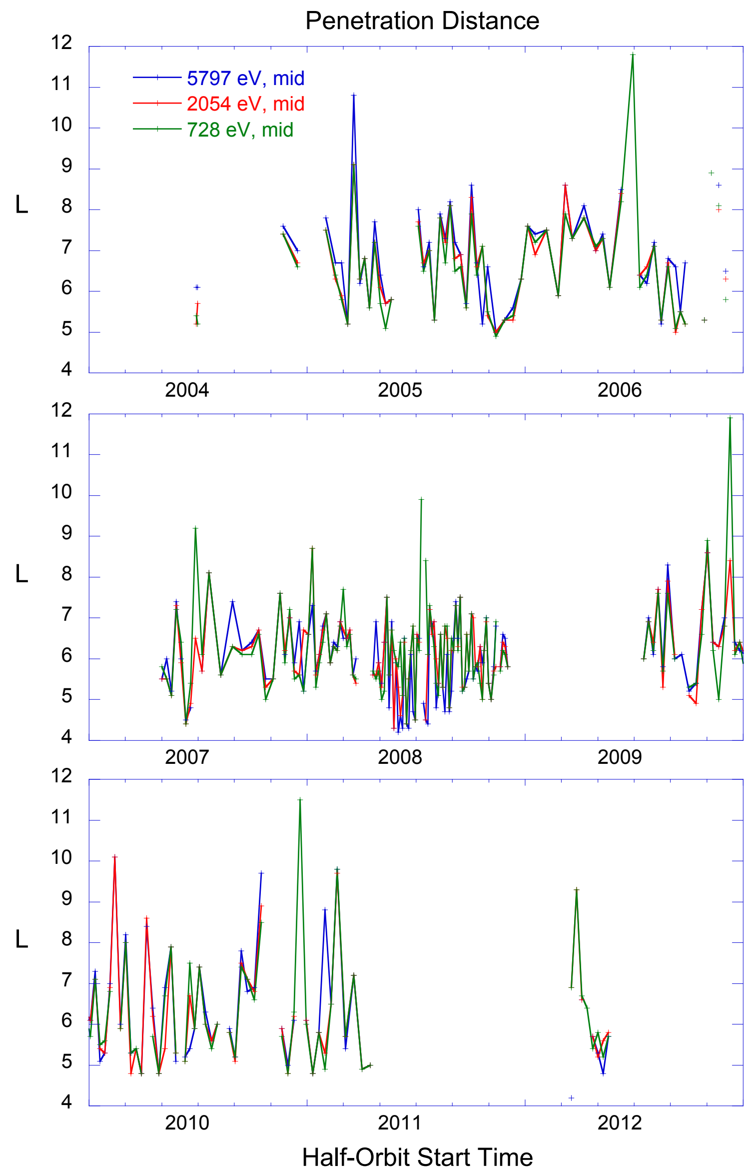

Penetration Distance
5797 eV, mid
2054 eV, mid
728 eV, mid
L
12
11
10
9
8
7
6
5
4
2004
2005
2006
2007
2008
2009
2010
2011
2012
Half-Orbit Start Time

Figure 6.

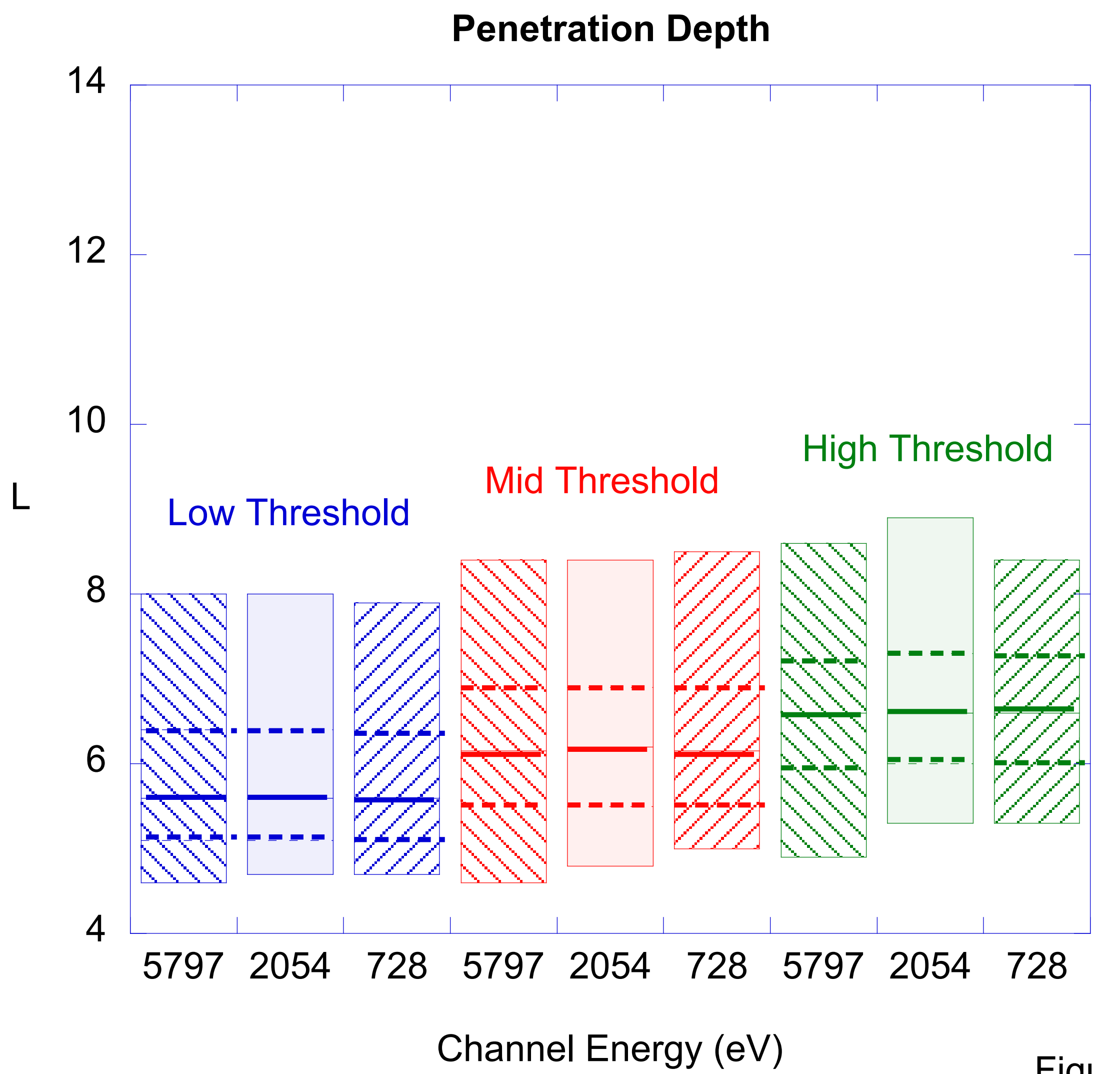
Penetration Depth
14
12
10
8
6
4
L
Low Threshold
Mid Threshold
High Threshold
5797
2054
728
5797
2054
728
5797
2054
728
Channel Energy (eV)

Figure 7.

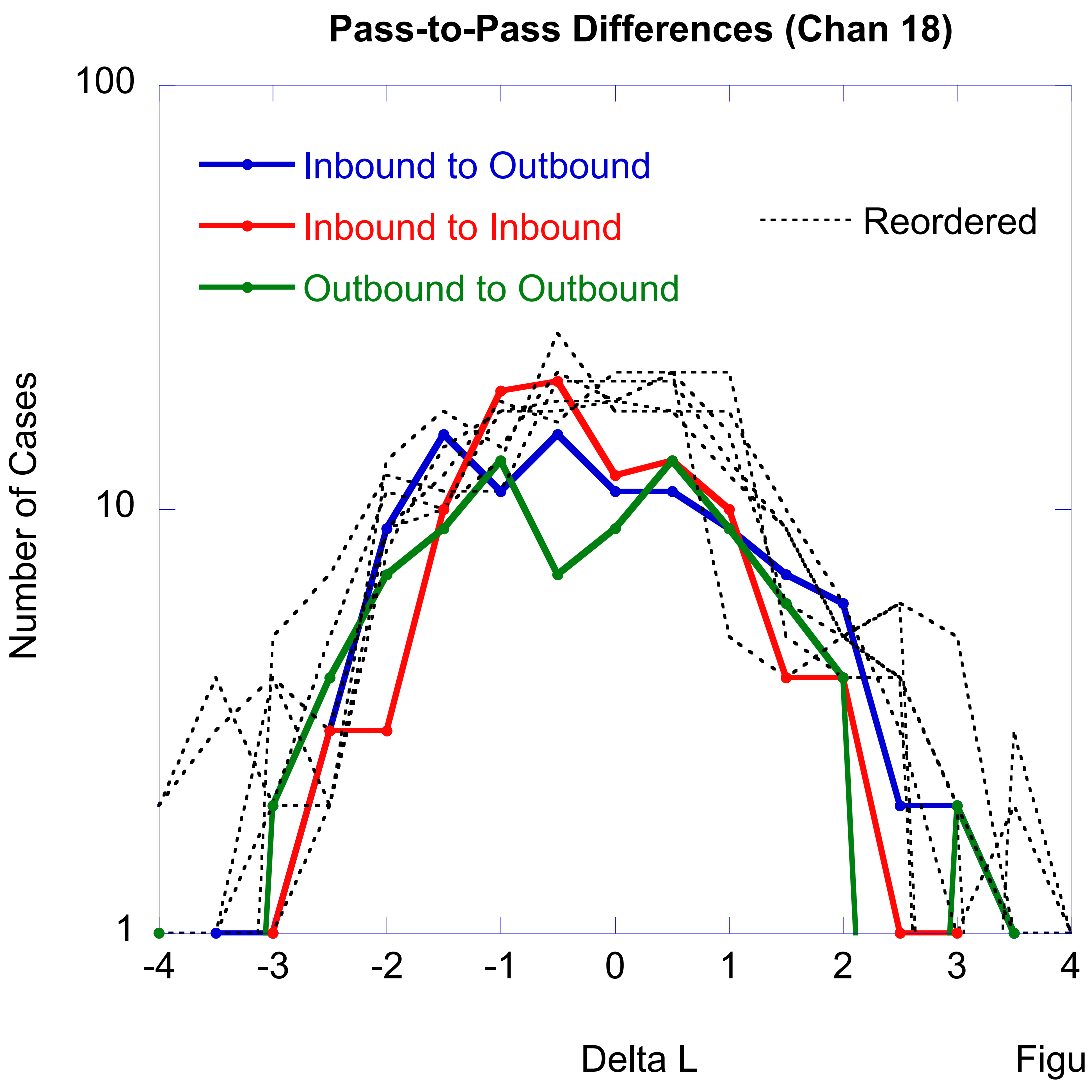

Pass-to-Pass Differences (Chan 18)
100
10
1
Number of Cases
-4
-3
-2
-1
0
1
2
3
4
Delta L
Inbound to Outbound
Inbound to Inbound
Outbound to Outbound
Reordered

Figure 8.

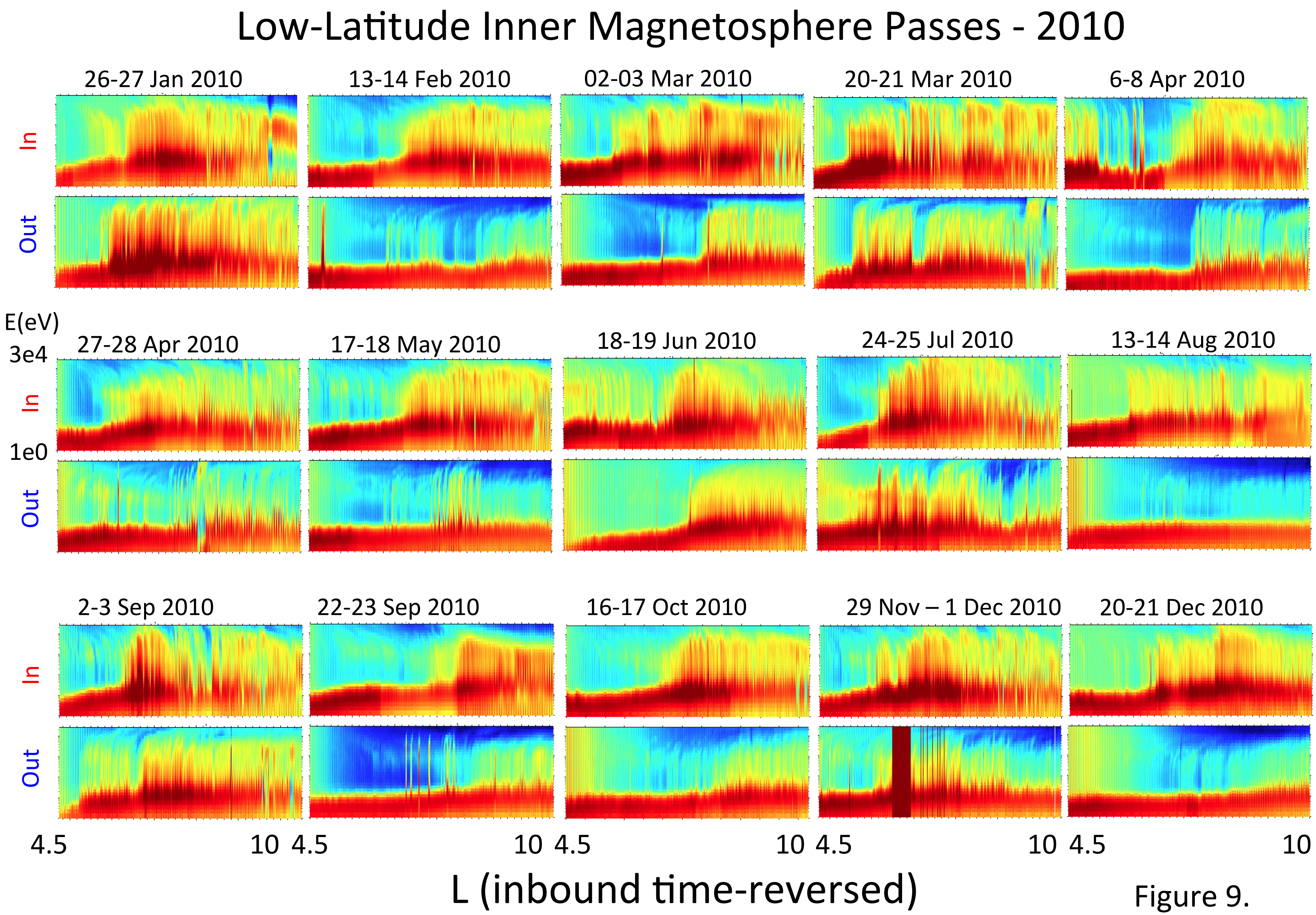
Low-Latitude Inner Magnetosphere Passes - 2010
26-27 Jan 2010
13-14 Feb 2010
02-03 Mar 2010
20-21 Mar 2010
6-8 Apr 2010
In
Out
E(eV)
3e4
1e0
27-28 Apr 2010
17-18 May 2010
18-19 Jun 2010
24-25 Jul 2010
13-14 Aug 2010
2-3 Sep 2010
22-23 Sep 2010
16-17 Oct 2010
29 Nov – 1 Dec 2010
20-21 Dec 2010
4.5
10
L (inbound time-reversed)

Figure 9.

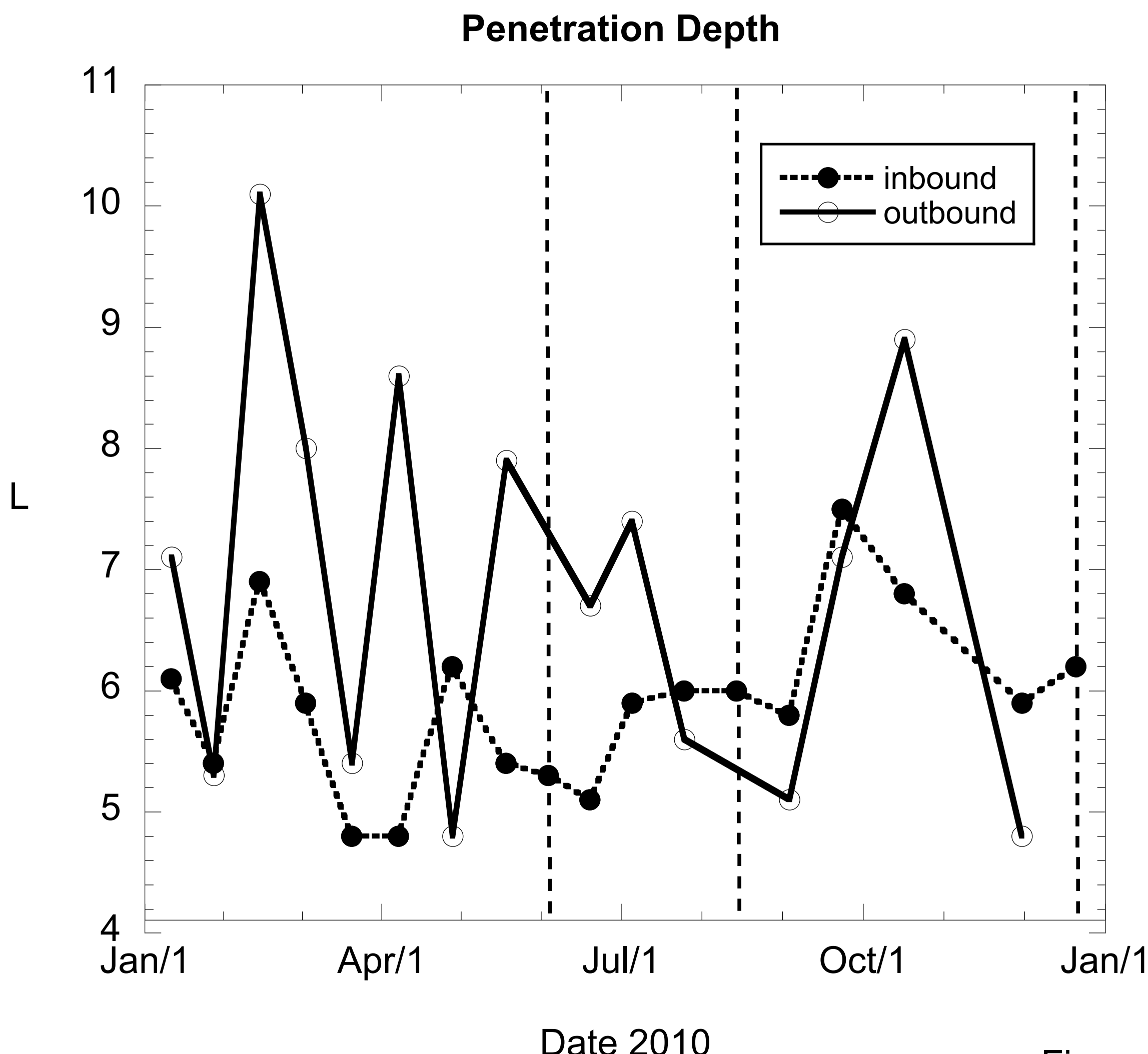
Penetration Depth
11
10
9
8
7
6
5
4
L
inbound
outbound
Jan/1
Apr/1
Jul/1
Oct/1
Jan/1
Date 2010

Figure 10.

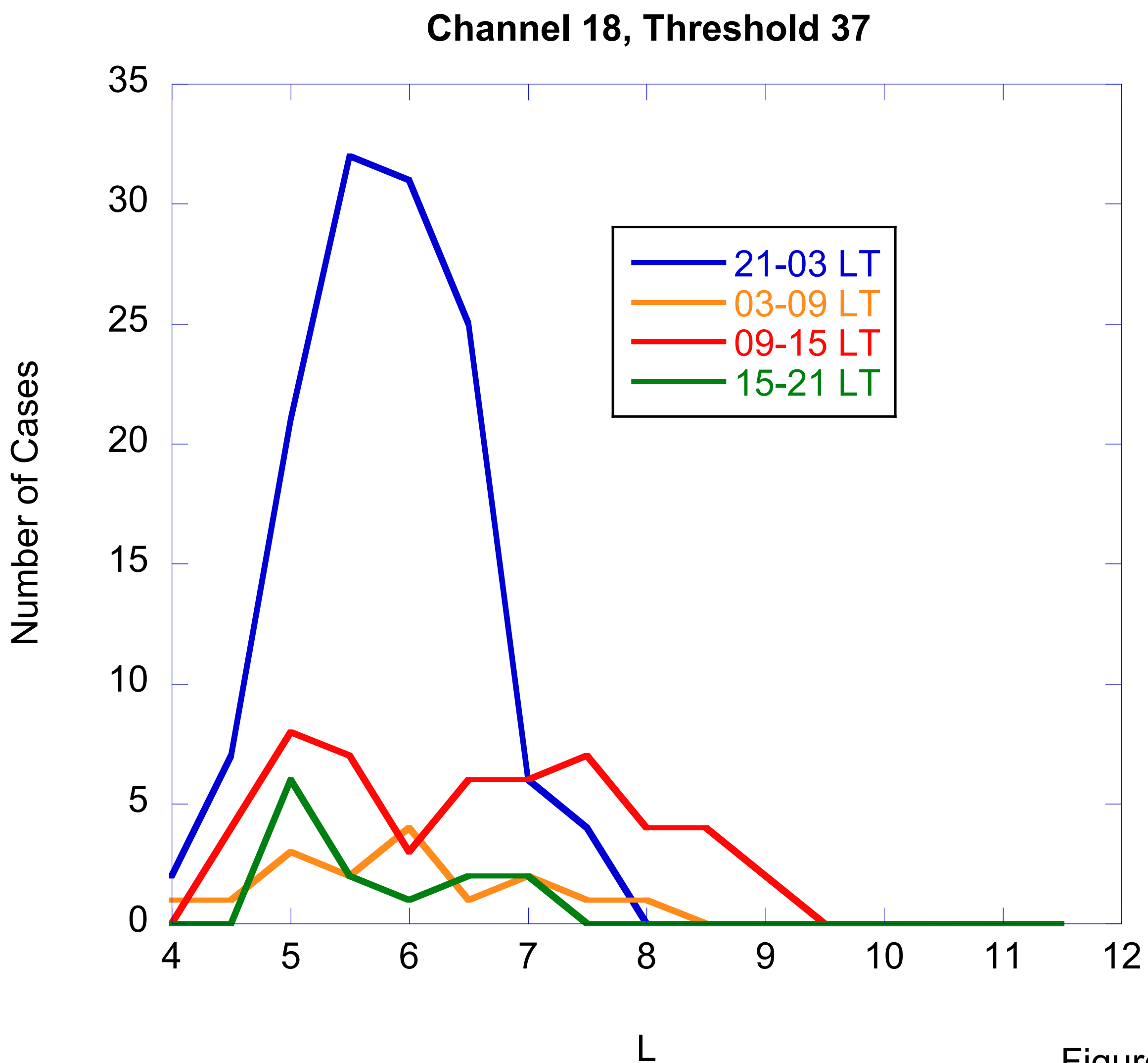
Channel 18, Threshold 37
Number of Cases
L
21-03 LT
03-09 LT
09-15 LT
15-21 LT
0
5
10
15
20
25
30
35
4
5
6
7
8
9
10
11
12

Figure 11.

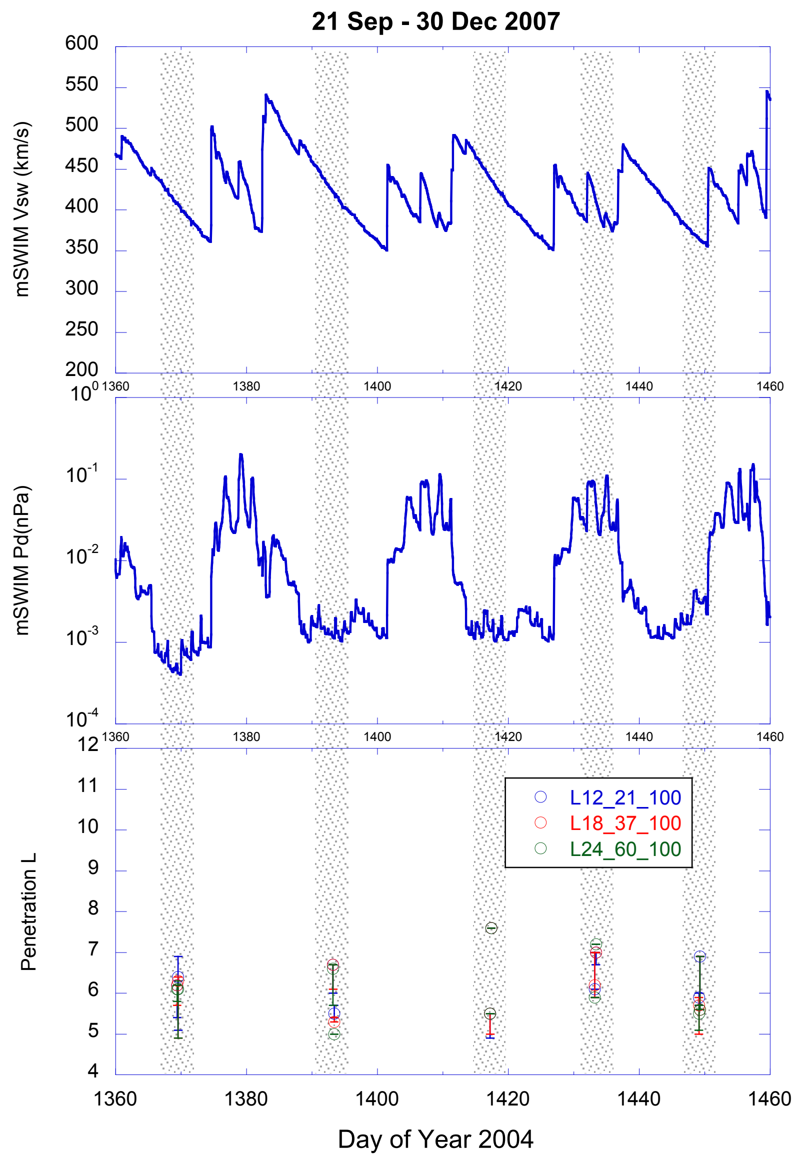

21 Sep - 30 Dec 2007
mSWIM Vsw (km/s)
600
550
500
450
400
350
300
250
200
1360
1380
1400
1420
1440
1460
mSWIM Pd(nPa)
10^{0}
10^{-1}
10^{-2}
10^{-3}
10^{-4}
Penetration L
12
11
10
9
8
7
6
5
4
L12_21_100
L18_37_100
L24_60_100
Day of Year 2004

Figure 12.

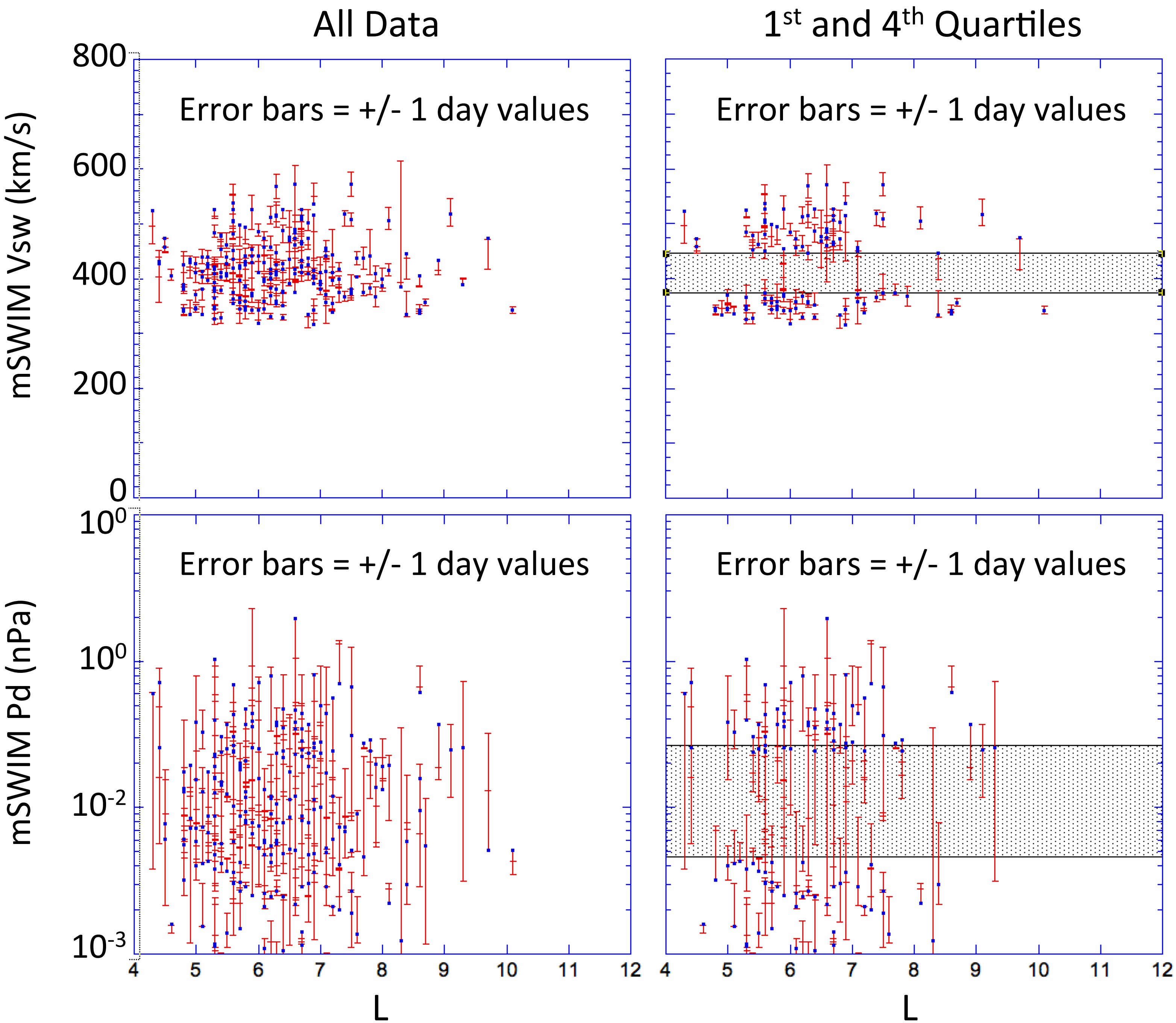
All Data
1st and 4th Quartiles
Error bars = +/- 1 day values
mSWIM Vsw (km/s)
800
600
400
200
0
mSWIM Pd (nPa)
10^0
10^0
10^-2
10^-3
4
5
6
7
8
9
10
11
12
L

Figure 13.